Acta Materialia 150 (2018) 130–138

Contents lists available at ScienceDirect

Acta Materialia

journal homepage: www.elsevier.com/locate/actamat

Full length article

Fracture behavior of heterogeneous nanostructured 316L austenitic stainless steel with nanotwin bundles

L. Xiong [a, 1], Z.S. You [b, 1], S.D. Qu [b], L. Lu [a, *]

[a] Shenyang National Laboratory for Materials Science, Institute of Metal Research, Chinese Academy of Sciences, 72 Wenhua Road, Shenyang 110016, People's Republic of China
[b] Herbert Gleiter Institute of Nanoscience, Nanjing University of Science and Technology, 200 Xiaolingwei Street, Nanjing 210094, People's Republic of China

ARTICLE INFO

Article history:
Received 15 August 2017
Received in revised form
20 February 2018
Accepted 22 February 2018
Available online 9 March 2018

Keywords:
Austenitic stainless steel
Nanotwins
Fracture toughness
Crack bridging
Strength-toughness synergy

ABSTRACT

The fracture behavior was investigated of a bulk nanostructured 316L austenitic stainless steel with embedded nanotwin bundles incorporated by dynamic plastic deformation. The nanotwin bundles were demonstrated to be critical to strengthen and toughen the as-deformed samples with mixed microstructures of nano-grains and nano-twins. With increment in strength, the fracture toughness decreases due to the generation of increasingly more nano-grains. Additional controlled thermal annealing that makes the nano-grains recover or recrystallize leads to reduced strengths but more remarkably improved fracture toughness. The enhanced strength–fracture toughness synergy can be attributed to the nanotwin bundles that constrict the damage development in the matrix of either nano-grains or recrystallized grains, and that resist crack propagation via acting as ductile crack bridging ligaments.

1. Introduction

Industrial applications of austenitic stainless steels (SS) with high resistances to corrosion and to oxidation are substantially limited by their relatively low yield strengths (less than 300 MPa in coarse-grained state) [1,2]. To strengthen the austenitic steels, refining grains into the sub-micron or even the nanometer scale by severe plastic deformation has recently been recognized as one of effective strategies [3–8]. Due to the low stacking fault energies of austenitic steels, deformation twinning usually acts as a dominant mechanism of microstructural refinement [9,10]. As a consequence, heterogeneous microstructures are generally produced with numerous bundles of deformation twins with spacing of several tens of nanometers embedded in a matrix of nanoscale grains [11,12]. The combined microstructure with nanotwins and nanograins contributes to ultra-high yield strengths. For instance, the yield strength of 316L SS has been increased to about 1.3 GPa by introducing a volume fraction of ~24% nanotwins through dynamic plastic deformation (DPD), and the strength of nanotwins themselves was estimated to be ~2.0 GPa [8]. However, due to the high-density dislocations accumulated at the twin boundaries (TBs) and within the tiny grains, the strain hardening capability and the uniform tensile ductility were severely reduced [8].

Thermal annealing is effective to further modify the microstructure to regain the tensile ductility and to optimize the strength-ductility synergy [13–15]. Comparing with the unstable nanograins associated with high excess energy, the bundles of nanoscale twins in the DPD samples are more stable during thermal treatment owing to the much lower interface energy of TBs [16,17]. Therefore, the nanotwin bundles are generally survived and the nanograins are replaced by recrystallized dislocation-free coarse grains [8,18]. This generates a unique coarse-grained austenitic structure reinforced by remanent strong nanotwins, exhibiting a combination of high strength and good tensile ductility [18,19].

Besides the strength and ductility, most engineering applications desire the materials to possess sufficient damage tolerance as well [20]. There are several microstructural and mechanical features which allude to the fact that the nanotwin bundles may also act as an ideal toughening "phase" to improve fracture resistance. The coherent TBs not only impede dislocation motion, but also react in various ways with impingent dislocations to effectively prevent stress concentration along them [21–24]. Moreover, both the embedded nanotwin bundles and the matrix are austenite, which do not create any abrupt phase boundaries where stress

* Corresponding author.
E-mail address: llu@imr.ac.cn (L. Lu).
[1] Equal contribution.

https://doi.org/10.1016/j.actamat.2018.02.065
1359-6454/

intensification may build up and cracks nucleate easily. The steels are in fact spatially homogeneous with respect to the chemical compositions and the elastic properties [19]. Further transmission electron microscope (TEM) observations have verified that the nanotwin bundles could coherently deform with the surrounding matrix [25]. Qin et al. [26,27] revealed in a nanostructured DPD Cu that the nanotwin bundles increase crack advancement resistance by generating coarse and deep ductile dimples. However, the underlying fracture and toughening mechanisms associated with the nanotwin bundles are still far from well understood.

In this study, fracture toughness tests were conducted on a nanotwinned 316L SS produced by DPD with different strains and with additional thermal annealing at different temperatures, which result in nanotwin bundles embedded in the matrix of deformed nano-grains and recrystallized micron-sized grains, respectively. The fracture behavior of the nanotwinned 316L SS was quantified in terms of *J*-integral fracture resistance curves that were accurately determined using miniaturized fracture specimens with the aid of a contactless crack opening displacement gauge developed recently [28]. Specific focus will be devoted to reveal the underlying toughening mechanism whereby the nanotwin bundles resist damage evolution in the nano-grain matrix, and to develop thermal treatment technique that optimizes the strength-fracture toughness synergy.

2. Experimental details

A commercial AISI 316L SS with a composition of Fe-16.42Cr-0.02C-0.37Si-1.42Mn-0.011S-0.040P (wt.%) was used in this study. The as-received steel was firstly annealed at 1200 °C for 1 h to generate uniform coarse austenite with an average grain size of ~100 μm, and then subjected to DPD at ambient temperature. The setup and processing parameters of the DPD facility have been described elsewhere [11,12]. To produce nanostructures with different volume fractions of deformation nanotwin bundles, the DPD treatment was repeated multiple times to obtain a few samples with plastic strains of 0.4, 0.8, 1.2 and 1.6, respectively. These imposed strains are defined as $\varepsilon = \ln(h_i/h_f)$, where h_i and h_f are the initial and final thicknesses of the DPD samples, respectively. The final geometric dimension of all DPD samples is about 35 mm in diameter and 4.5 mm in thickness. To further modify the microstructure, the $\varepsilon = 1.6$ samples were annealed at 710, 720 and 730 °C for 20 min and then water quenched.

For the fracture toughness tests, miniaturized compact tension (CT) specimens were cut from the deformed DPD disks by electrical discharge machining (EDM). As Fig. 1 shows, only specimens with crack plane perpendicular to tangential direction (TD) and crack growth direction parallel to radial direction (RD) were tested, due to the limited thickness of the current DPD samples. The fracture specimens had a width, *W*, of 8 mm, a thickness, *B*, of 4 mm, and an initial notch depth of ~3.2 mm. To produce sharp crack tips, the specimens were further fatigue pre-cracked under cyclic tension-tension loading until a total crack length of ~4.0 mm (~0.5 W) was obtained. Because pronounced crack tunneling is inevitably present as the crack advances in planar miniaturized CT specimen with the same dimension, invalidating the obtained fracture resistance curves [28], side grooves with a total depth of 0.2B were additionally machined on both surfaces of the fatigue pre-cracked CT specimens to enhance the surface stress constraint and make the crack extend straightly.

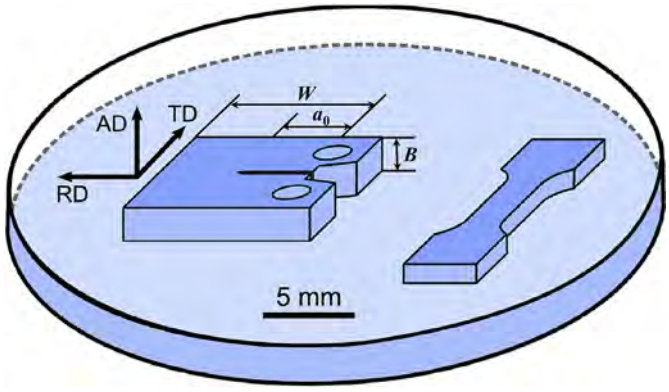

Fig. 1. Schematic illustration of the specimens for fracture toughness and tensile tests and their orientations in the DPD disc. The coordinate axes are denoted as axial direction (AD), radial direction (RD) and tangential direction (TD). Thus, the CT fracture specimen is in T-R orientation and the tensile direction is parallel to RD.

The fracture tests were carried out on an Instron 5982 testing machine with a load capacity of 5 kN under displacement control. The cross-head speed was 0.1 mm/min. The load-line displacements of the miniaturized CT specimens were determined by measuring the crack mouse opening displacements using a custom-designed contactless video crack opening displacement (VCOD) gauging system, which has been described in details in Ref. [28]. The VCOD gauge exhibits a high accuracy and thus enables the determination of instantaneous crack length by using the unloading compliance technique [28]. The conventional single specimen technique was employed to determine the elastic-plastic *J*-integral fracture resistance curve, following the procedure recommended in the ASTM standard E1820 [29].

Uniaxial tensile tests were performed on an Instron 5848 Microtester with a strain rate of ~3×10^{-3} s^{-1} at ambient temperature. The tensile specimens had a length of 5 mm, a width of 1 mm, and a thickness of 0.5 mm in the gauge section. As shown in Fig. 1, the tensile axis corresponds to the principal loading direction (TD) of the CT specimens. A contactless MTS LX300 laser extensometer was used to measure the tensile strain upon loading. At least three tensile tests were performed to guarantee the repeatability.

Microstructure of the DPD and the annealed samples were characterized by a JEOL 2010 TEM operated at an accelerating voltage of 200 kV. The fracture surfaces were examined by a FEI NovaSEM 430 field emission gun scanning electron microscope (SEM) under secondary electron imaging mode. An Olympus LEXT OLS4000 confocal laser scanning microscope (CLSM) was used to determine the three dimensional morphologies of the fracture surfaces.

3. Results

3.1. Microstructures and tensile behavior

The microstructural features and tensile properties after DPD treatement and subsequent thermal annealing of 316L SS have been thoroughly investigated by Yan et al. [7,8]. In samples with $\varepsilon = 0.4$, over 60% of original coarse grains are occupied by nanoscale deformation twins with an average twin spacing of ~40 nm and the rest by dislocation structures [30]. With ε increasing from 0.4 to 1.6, the volume fraction of the nanotwinned regions decreases from $60 \pm 10\%$ to $26 \pm 5\%$. Fig. 2a displays the remanent bundles of deformation twins at $\varepsilon = 1.6$ (marked by the dash lines) embedded in the nanograin matrix. The average widths of the nanotwin bundles, ranging from sub-micrometer to micrometers, is ~5.5 μm, while the average length is ~15 μm. High density of dislocations accumulated at most TBs with a mean twin spacing of ~16 nm (Fig. 2b). In the matrix, most nanograins are elongated along the shear bands, with an average transverse size of ~30 nm and a mean longitudinal size of ~80 nm (Fig. 2c).

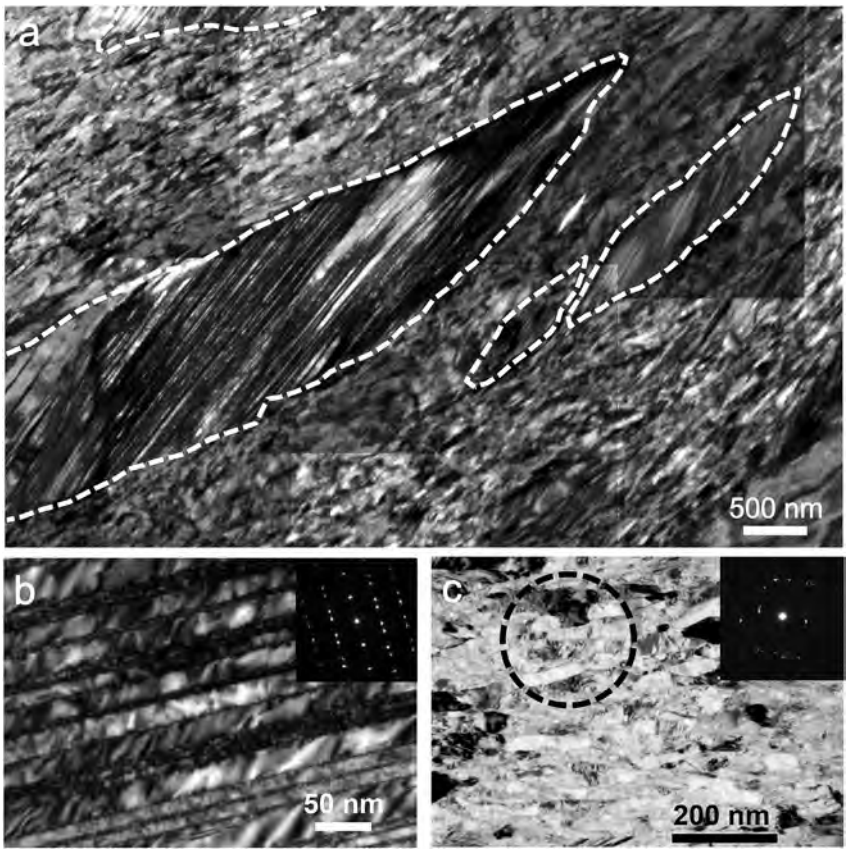

Fig. 2. (a) Typical TEM observations of the cross-sectional microstructure of DPD 316L SS with $\varepsilon = 1.6$, showing nanotwin bundles (enclosed by white dash lines) embedded in a matrix of nanograins. (b) Nanoscale deformation twins with a high density of dislocations accumulated at the TBs and the corresponding selected area electron diffraction (SAED) pattern. (c) Detailed observations on the elongated nanograin matrix and the SAED pattern of the dash circle area.

Thermal annealing at temperatures ranging from 710 to 730 °C leads to evident microstructural variations of the $\varepsilon = 1.6$ samples. Fig. 3 shows the typical microstructure of DPD sample annealed at 720 °C. The nanotwin bundles survived after the annealing, without detected variation in twin spacing; but the densities of the accumulated dislocations at the TBs were substantially reduced comparing with the deformed state [8,31]. However, the GBs in the nanograined matrix were substantially recovered and parts of nanograins were even recrystallized and had grown to micron-sized defect-free grains. The average grain size increases from 150 nm to 550 nm as the annealing temperature is elevated from 710 to 730 °C.

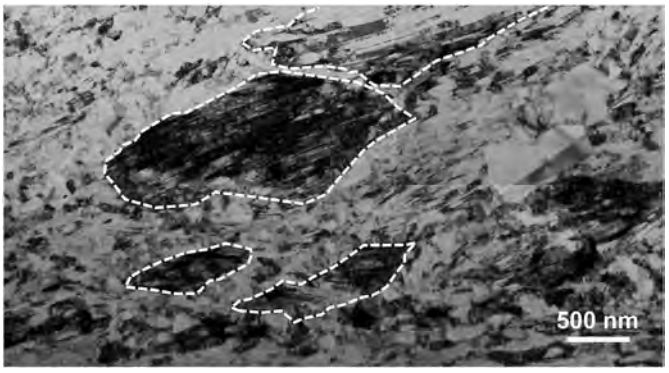

Fig. 3. TEM characterization of the cross-sectional microstructure of $\varepsilon = 1.6$ DPD 316L SS annealed at 720 °C for 20 min, showing remained nanotwin bundles (enclosed by white dash lines) embedded in the matrix of recovered or recrystallized grains.

The yield strength σ_{ys} and the ultimate tensile strength σ_{uts} were improved from 275 ± 5 MPa and 585 ± 9 MPa at the coarse grained state to 920 ± 20 MPa and 962 ± 20 MPa at $\varepsilon = 0.4$, while the elongation to failure δ_f was decreased to 15 ± 1%. Increment in ε further elevates substantially both σ_{ys} and σ_{uts}. All DPD samples exhibit limited uniform elongations (~1%), due to the diminished strain hardening capability. The subsequent thermal annealing leads to a slight decrease in strengths and evident enhancement in tensile ductility. For instance, after annealing at 730 °C for 20 min, σ_{ys} and σ_{uts} were reduced to 1020 ± 15 MPa and 1115 ± 15 MPa, respectively, while δ_f was elevated to 18 ± 1%. The tensile properties of the as-DPD and the annealed DPD samples are summarized in Table 1.

3.2. Fracture toughness

Fig. 4a and b shows the representative force P versus load-line displacement v curves before instable crack propagation for DPD 316L SS with different ε and the $\varepsilon = 1.6$ samples annealed at different temperatures, respectively. It is evident that the ratios of maximum force P_{max} to P_Q are larger than 1.1, with P_Q the point where a line having a slope 95% of the slope of the tangent to the initial linear part intersects the P-v curve. This is caused by the substantial crack tip plastic deformation before crack extension, and invalidates the linear-elastic plane strain conditions for directly determining the critical stress-intensity factor K_{IC} [32]. Therefore, elastic-plastic fracture mechanics method based on J-integral was employed instead to evaluate their fracture toughness.

The computed J-integral fracture resistance curves (J-R curves),

Table 1
Microstructural composition, tensile properties, and fracture toughness of the DPD 316L SS with different ε and the $\varepsilon = 1.6$ sample annealed at different temperatures. The tensile properties of coarse-grained (CG) counterpart is included for comparison.

Sample	V_{NT} (%)	V_G (%)	σ_{ys} (MPa)	σ_{uts} (MPa)	δ_f (%)	J_{IC} (kJ m^{-2})	K_{JC} (MPa m$^{1/2}$)	a_c (mm)	K^*_{JC} (MPa m$^{1/2}$)
$\varepsilon = 0.4$	60 ± 10	–	920 ± 20	962 ± 20	15 ± 1	84 ± 4	132 ± 3	6.6	126-177 [30]
$\varepsilon = 0.8$	49 ± 8	51 ± 8	1110 ± 22	1159 ± 20	10 ± 1	44 ± 3	96 ± 4	2.4	
$\varepsilon = 1.2$	31 ± 7	69 ± 7	1308 ± 50	1358 ± 50	8 ± 1	30 ± 2	79 ± 3	1.2	
$\varepsilon = 1.6$	26 ± 5	74 ± 5	1366 ± 49	1416 ± 50	8 ± 1	27 ± 6	76 ± 8	1.0	117 ± 1 [31]
710 °C Annealed	28 ± 2	72 ± 2	1144 ± 39	1294 ± 56	13 ± 2	43 ± 5	95 ± 6	2.2	136 ± 4 [31]
720 °C Annealed	23 ± 6	77 ± 6	1113 ± 55	1222 ± 8	14 ± 1	59 ± 3	111 ± 3	3.2	151 ± 8 [31]
730 °C Annealed	21 ± 2	79 ± 2	1020 ± 15	1115 ± 15	18 ± 1	91 ± 9	138 ± 7	5.8	172 ± 5 [31]
CG	–	–	275 ± 5	585 ± 9	67 ± 4	–	–		
CG [43]	–	–	200–300	–	–	215–800	210–400	460	

V_{NT}, volume fraction of nanotwin bundles; V_G, volume fraction of nanograins or recrystallized grains; σ_{ys}, yield strength; σ_{uts}, ultimate tensile strength; δ_f, elongation to failure; J_{IC}, critical J-integral; K_{JC}, critical stress intensity factor computed from J_{IC}; $a_c = K^2_{JC}/\pi\sigma^2_{ys}$, transition crack size between plastic yield and fracture; K^*_{JC}, critical stress intensity factor computed from J_{IC} obtained by single-edge notched bending tests [30,31].

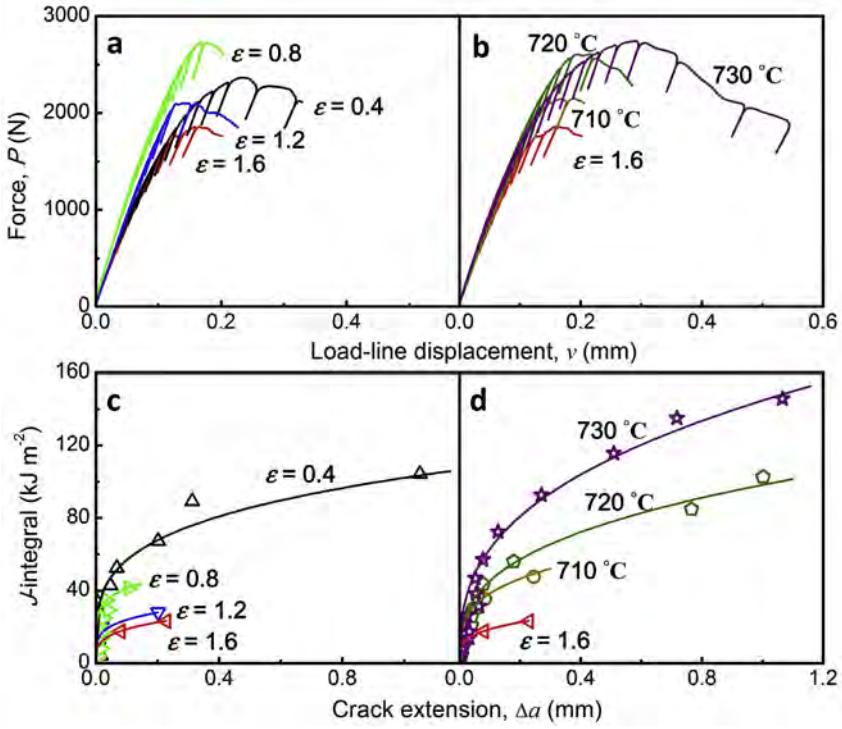

Fig. 4. Typical curves of force P versus load-line displacement v for (a) the as-DPD 316L SS with different ε and (b) the $\varepsilon = 1.6$ 316L SS annealed at different temperatures for 20 min. The unloading compliance technique was applied to determine the instantaneous crack length. (c, d) Variation of J-integral as a function of crack extension Δa calculated from the data in (a, b), respectively.

namely variation of J-integral as a function of crack extension Δa, for the as-DPD and annealed DPD samples are displayed in Fig. 4c and d, respectively. For the samples ($\varepsilon = 0.4$ and the annealed samples) that exhibit stable crack extension, the provisional critical J-integral value J_Q is taken as the intersection of the J-Δa curve with the 0.2 mm offset blunting line ($J = 2\sigma_Y \Delta a$, where σ_Y is the average value of σ_{ys} and σ_{uts} from the tensile tests). For the other samples ($\varepsilon = 0.8/1.2/1.6$) in which the cracks unstably extend before Δa exceeds 0.2 mm, the J-integral at the point of unstable crack extension is taken as J_Q.

Both the net sample thickness B_N (~3.2 mm) and the initial crack ligament $b_0 = W - a_0$ (~4 mm) are larger than the quantity $25J_Q/\sigma_Y$, and the side-grooves guarantee straight crack extension in such miniaturized specimens [28]. Therefore, J_Q for all the samples can be quantified as the size-independent fracture toughness J_{IC} that is an intrinsic material property representing the crack initiation resistance [29]. The corresponding critical stress intensity factor K_{JC} can be calculated by using the following relationship:

$$K_{JC} = \sqrt{\frac{EJ_{IC}}{1-\nu^2}} \quad (1)$$

where for 316L SS the Young's modulus $E = 193$ GPa, and the Poisson's ratio $\nu = 0.3$. The measured J_{IC} and the calculated K_{JC} values are summarized in Table 1.

The $\varepsilon = 0.4$ sample with a yield strength of 920 MPa possesses a K_{JC} of 132 ± 3 MPa m$^{1/2}$, in consistent with our previous measurement obtained by three point bending fracture test (exceeding 126 MPa m$^{1/2}$ based on crack tip opening displacement analysis) [30]. For the as-DPD sample, K_{JC} gradually decreases to 76 ± 8 MPa m$^{1/2}$ at $\varepsilon = 1.6$, accompanied by increment in yield stress to ~1366 MPa. After further annealing of $\varepsilon = 1.6$ sample at 730 °C for 20 min, the K_{JC} is remarkably elevated to 138 ± 7 MPa m$^{1/2}$, while σ_{ys} is still as high as 1.0 GPa. The result indicates that the synergy of

strength and fracture toughness for nanostructured 316L SS has been enhanced after thermal annealing.

Table 1 also lists the literature data of the fracture toughness obtained through fracture tests of single-edge notched bend (SENB) specimens with 2 mm thickness [30,31]. Obviously, the K_{JC} in this study are much smaller than those of SENB on the same specimens in Refs. [30,31]. This discrepancy mainly arises from crack tunneling (faster crack propagation in the specimen center) in SENB tests, which inevitably occurs in the miniaturized fracture specimens without side-grooves [28]. The crack tunneling results in a more precipitous increment in J-integral as the crack extends [28] and therefore specimen-dependent over-estimations of J_{IC} and K_{JC} at a certain extent. In contrary to the SENB tests, side-grooved CT tests satisfy both the specimen size and the straight crack front requirements. Therefore, the K_{JC} in this investigation can represent the intrinsic fracture toughness of the new 316L SS.

4. Discussion

4.1. Fractography and the toughening mechanism

The combination of high strength and considerable fracture toughness in the DPD nanostructured 316L SS is intimately correlated with its heterogeneous microstructure, especially the presence of nanotwin bundles as a unique reinforcement phase. To get insight of the underlying failure and toughening mechanisms associated with the nanotwin bundles, the fracture surfaces were carefully examined.

Homogeneous equiaxed coarse dimples with diameters larger than 20 μm are observed on the fracture surface (Fig. 5a) in the DPD sample with $\varepsilon = 0.4$, consisting solely of deformation twins and dislocation structures. On the contrary, the fracture surfaces of the DPD samples with $\varepsilon > 0.4$ are even more heterogeneous. As shown in Fig. 5b, in addition to numerous elongated coarse dimples, many equiaxed fine dimples are seen in the $\varepsilon = 1.6$ samples. The statistic results as listed in Table 2 show that the area fraction of coarse dimples is reduced from 39% to 26%, synchronized with the decrement in volume fraction of nanotwins as ε increases from 0.8 to 1.6. It has been recognized that the fine dimples arise from the failure of the nano-grain matrix, and the coarse dimples are associated with nanotwins [26,27]. Analogous fine dimples were frequently detected in previous studies on the fracture of homogeneous nanocrystalline materials [33,34]. The mean diameter of these fine dimples is about ~5 μm (Table 2), about two orders of magnitude larger than the average grain size (~30 nm).

In order to investigate the fracture path, further fractographic analysis was carried out on the matching fracture surfaces of CT specimens. Fig. 6a and b are the SEM pictures showing pairs of coarse and fine dimples on the two halves of the fractured DPD sample with $\varepsilon = 1.6$, and Fig. 6c and d displays the CLSM three dimensional topographies of the same areas. A close examination revealed that all the fine dimples have a 'cup-cup'-like concave contour, suggesting a ductile fracture behavior involving void nucleation, growth and coalescence. But distinction happens for the coarse dimples on the two mating fracture surfaces, which exhibit obviously concave and convex contours, as illustrated in Fig. 6c and d.

Table 2
Volume fraction (V), longitudinal size (L) of coarse and fine dimples of the DPD 316L SS with different ε and the $\varepsilon = 1.6$ sample annealed at different temperatures.

Sample	Coarse dimples		Fine dimples	
	V (%)	L (μm)	V (%)	W (μm)
$\varepsilon = 0.8$	39 ± 4	34	61 ± 4	6
$\varepsilon = 1.2$	32 ± 2	37	68 ± 2	5
$\varepsilon = 1.6$	26 ± 3	31	74 ± 3	5
710 °C annealed	31 ± 3	44	69 ± 3	8
720 °C annealed	29 ± 5	40	71 ± 5	9
730 °C annealed	32 ± 7	41	68 ± 7	9

The above inspection on fracture surfaces leads to the conjecture that the nanotwin bundles are pulled out from the nano-grain matrix during fracture. To further support this point, a DPD sample with $\varepsilon = 1.6$ was loaded up to a point where the crack had propagated a certain distance and then unloaded. The crack front was delineated by further fatigue at a low stress intensity factor amplitude. As shown in Fig. 7a, the areas broken by post-fatigue are very smooth, and their boundaries represent a microscopically tortuous crack front line (white dash line in Fig. 7a). Some smooth areas, entirely surrounded by small dimples, can also be observed behind the crack front. The magnified observations in Fig. 7b and c compare the smooth islands just behind the crack tip and the elongated coarse dimples far from the crack tip. The analogous sizes and shapes suggest they are both associated with the nanotwin bundles. Since the smooth fracture surfaces are formed by post-fatigue, the nanotwin bundles close to crack tip are believed to still connect the two fracture surfaces, namely act as crack bridges, when the main crack propagates.

Based on the fracture surface analysis, the principle of crack propagation in the heterogeneous nanostructured 316L SS with embedded nanotwin bundles is depicted in Fig. 8. The initiation of fracture involves crack tip blunting by plastic deformation followed by micro-void formation and growth preferentially along the GBs and triple junctions of the nano-grain matrix ahead of the crack tip (Fig. 8a). The final coalescence of these micro-voids with the main

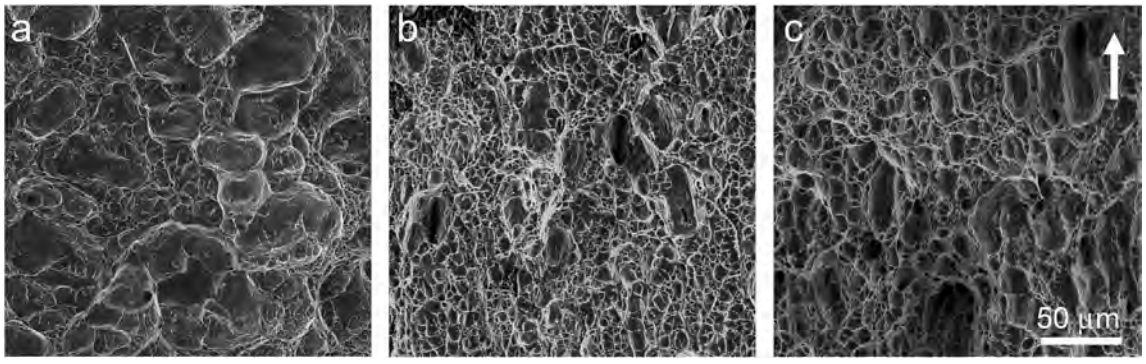

Fig. 5. SEM observations on the fracture surfaces of DPD 316L SS samples. (a) $\varepsilon = 0.4$; (b) $\varepsilon = 1.6$; (c) $\varepsilon = 1.6$ and annealed at 710 °C for 20 min. The arrow in (c) indicates the crack propagation direction.

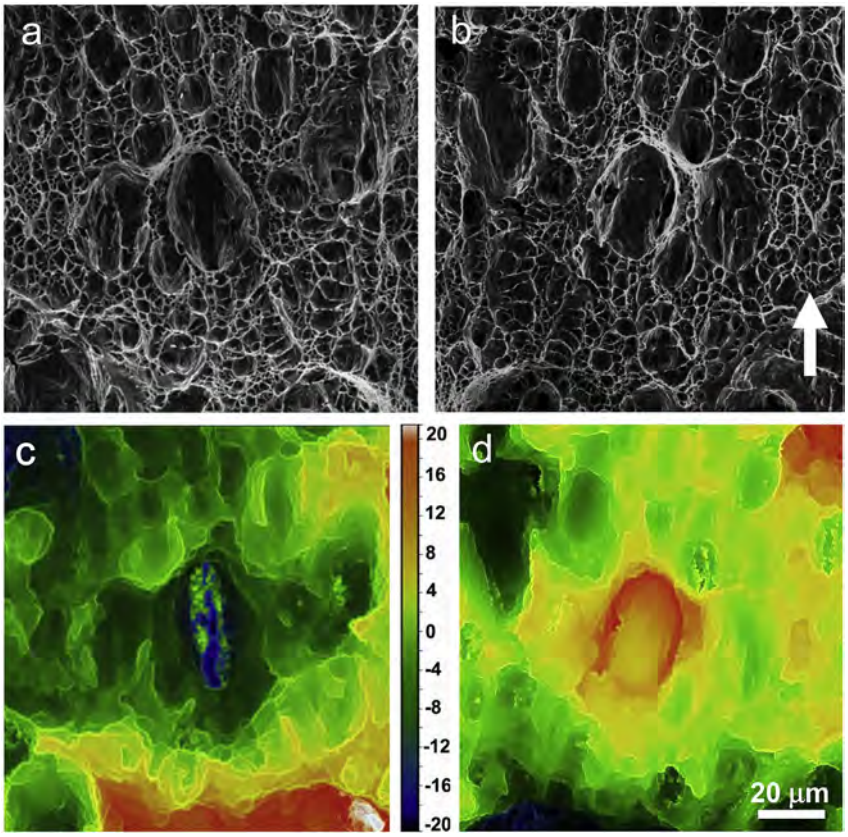

Fig. 6. (a, b) Fractographs taken from the same position on two halves of a broken specimen with $\varepsilon = 1.6$, showing pairs of coarse and fine dimples. (c, d) CLSM images of the same areas corresponding to (a, b), respectively, representing the three-dimensional morphologies of the coarse dimples. The color of (c, d) stands for the relative height as indicated in the color-bar in unit of μm. The arrow in (b) indicates the crack propagation direction.

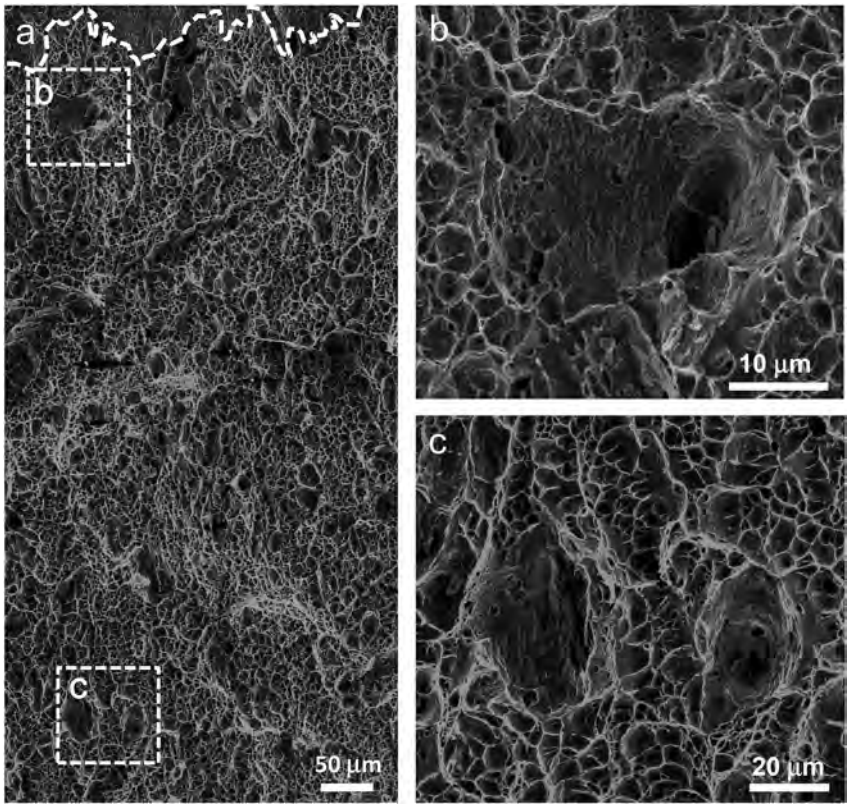

Fig. 7. (a) Fractographic observations on the area immediately close to the crack tip (white dash line) of the DPD 316L SS with $\varepsilon = 1.6$, which was delineated and opened by post-fatiguing at a low stress amplitude; (b) and (c), magnifications of the boxed areas in (a), showing the smooth islands among fine dimples just behind the crack tip and the elongated coarse dimples far from the crack tip, respectively.

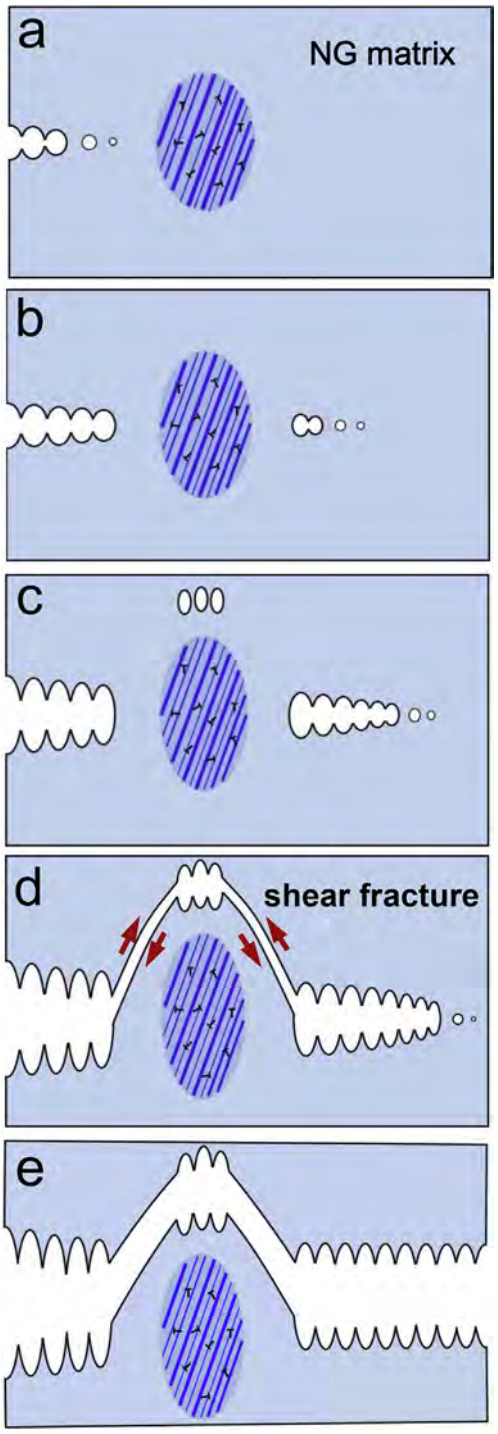

Fig. 8. Schematic illustrating the crack propagation processes in mixed microstructure with nanotwin bundles embedded in nano-grain (NG) matrix. (a) Voids nucleate and grow in the NG matrix. (b) Crack goes around the nanotwin bundle which then acts as a crack bridge resisting further crack growth. (c) Nanotwin bundle is tensioned and voids nucleate at its tip. (d) Shear fracture takes place some distance away from the nanotwin bundle and the nanotwin bundle is eventually pulled out. (e) Concave and convex coarse dimples form on the two halves of the broken specimen.

crack leads to a crack extension. Generation of analogous micro-voids is relatively difficult at TBs; therefore, the crack front goes around the confronted nanotwin bundles and leaves them as crack bridges in the wake of the main crack (Fig. 8b). The crack bridging zone with a nanotwin bundle is plastically tensioned as the crack

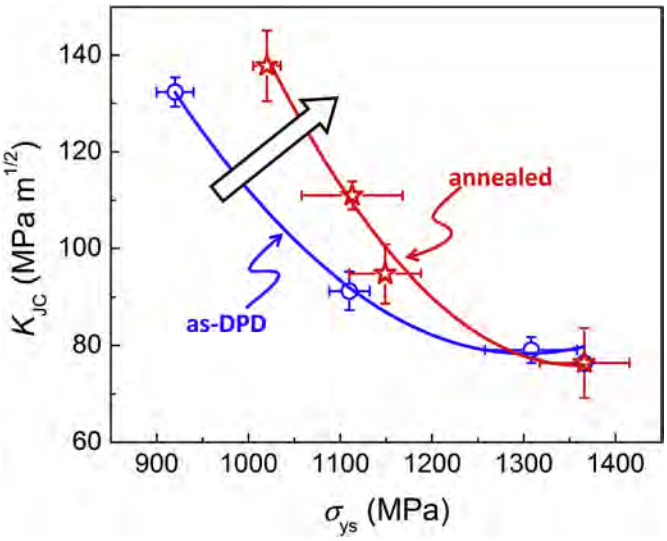

Fig. 9. Correlation of fracture toughness (K_{JC}) and yield strength (σ_{ys}) for the as-DPD and the annealed DPD 316L SS with nanotwin bundles.

further opens, until the moment at which micro-voids nucleate at the nano-grain region at the bottom of the nanotwin bundle (Fig. 8c). Eventually, shear fracture takes place also along the nano-grain region, away from the nanotwin bundle (Fig. 8d), and produces sunken and protrudent fracture surfaces on the two halves of a broken specimen (Fig. 8e), as evidenced by the CLSM observations in Fig. 8c and d.

The supposition that the sample always fails along the nano-grain regions is proposed based on the statistical results that the average width of the coarse dimples (~17 μm) is about three times larger than that of the nanotwin bundles (~5.5 μm). The scrutiny on the fracture behavior of 316L SS reveals the mechanical roles played by the nanotwin bundles are quite different from those by other reinforcement phases, such as hard second-phase particles or martensitic phases, whose interface or boundaries are generally preferential crack nucleation sites [35,36].

The toughening mechanism of nanotwin bundles can be considered from the following aspects. First, nanotwin bundles are not only strong but also ductile. The deformation of nanotwin bundles dissipates more irreversible plastic energy at the ahead of crack tip [21,37]. Second, as embedded in the nano-grain matrix, they may constrain strain localization in the nano-grains and discourage the nucleation and growth of voids. This is already proved by the detection of coarser dimples compared with fine dimples in homogeneous nanocrystalline metals. Third, as an extrinsic toughening mechanism, they act as ductile crack bridging segments, shielding crack tip stress concentration and thus resisting the crack propagation [38].

4.2. Influence of thermal annealing on strength-fracture toughness synergy

In general, fracture toughness decreases as the strength of a material increases [39]. As Fig. 9 shows, the fracture toughness K_{JC} of DPD 316L SS decreases with increasing yield strength σ_{ys} (the lower curve). Since the increment in strength arises from further microstructural refinement producing more GBs at nanometer scale, the reduction in K_{JC} is reasonable by taking account of the preferential micro-voids nucleation and growth in nanograined regions [40–42]. The larger the volume fraction of nanograins, the lower the irreversible plastic energy dissipated to extend the crack

and the lower the fracture toughness. However, in the contrary to the homogeneous nanocrystalline materials, the heterogeneous DPD 316L SS samples with nanotwin bundles guarantees a considerable fracture toughness (76 ± 8 MPa $m^{1/2}$) at a strength as high as ~1.4 GPa.

As discussed above, the high density of GBs are potential sites for void nucleation, which limits the fracture resistance. Subsequent thermal annealing induced grain coarsening may reduce the viod nucleation sites and further optimize the strength-toughness synergy. The upper curve in Fig. 9 demonstrates the effect of thermal annealing at different temperatures on the strength and fracture toughness of the DPD 316L SS with $\varepsilon = 1.6$. K_{JC} is remarkably restored after the controlled thermal annealing, and the strength-fracture toughness of the annealed samples are evidently shifted up and toward the right compared with those of the as-DPD samples, manifesting that the thermal annealing leads to a concurrent improvement in strength and fracture toughness. During thermal annealing, recovery or even recrystallization preferentially occurs in the nanograin matrix [8], and produces dislocation-free submicro- or micro-sized grains with less defected GBs. This process effectively reduces the density of micro-void nucleation sites. As Fig. 5c shows, two kinds of dimples are still visible on the fracture surface of the $\varepsilon = 1.6$ sample annealed at 710 °C. However, the dimple sizes turn out to be larger than those of the as-DPD samples (see Table 2).

As shown in Table 1, the fracture toughness of the nanotwinned 316L SS is much lower than that of the coarse-grained counterpart ($K_{JC} = 210–400$ MPa $m^{1/2}$, depending on various metallurgical and heat treatments [43,44]). In combination with the high strength, this in general substantially reduces the damage tolerance. The transition crack sizes between plastic yield and fracture of the 316L SS samples, defined as $a_c = K_{IC}^2/\pi\sigma_{ys}^2$, are also included in Table 1. Comparing with that of the coarse-grained counterpart (about 460 mm), the a_c values of the nanotwinned 316L SS are much smaller and drop to only a few millimeters, ranging from 1 to 6 mm. We have to admit that the limited a_c is an indication that the nanotwinned 316L SS turns out to be more sensitive to defects, which is generally true for many very high strength metallic materials [45]. This fact also points to the enormous importance of enhancing the fracture toughness that determines the real loading capacity (namely, $\sigma \propto K_{IC}/\sqrt{\pi a}$), once the crack is longer than a_c. In this respect, the 730 °C annealed sample predominately strengthened by nanotwin bundles is of advantage owing to the considerable fracture toughness (~140 MPa $m^{1/2}$).

This preliminary investigation evidently demonstrates the possibility to retain toughness upon strengthening by nanoscale twin structures. This unique behavior is practicable for many engineering metallic materials with low or medium stacking fault energies, in which a certain volume fraction of nanotwins can be easily produced by plastic deformation [19,46–48]. Many microstructural parameters associated with the nanotwin bundles, including volume fraction, bundle size, TB orientation, and spatial distribution, may also strongly influence their toughening effects, which deserve further deep investigations in the future.

5. Conclusion

The fracture characteristics of the austenitic 316L stainless steel with heterogeneous microstructure comprising of bundles of nanoscale deformation twins embedded in the matrices with hard nano-grains and with soft recrystallized micro-sized grains were assessed by elastic-plastic fracture mechanics based on *J*-integral. The nanotwin bundles play an important mechanical role in constricting void initiation in nano-grain matrix, along with resisting crack propagation by acting as crack bridging ligaments, which are beneficial to enhance the fracture resistance. Controlled thermal annealing results in the formation of recovered or recrystallized grains which replace the vulnerable nano-grains, and promotes the toughening effect due to the nanotwin bundles. The nanotwinned steel exhibits a considerable fracture toughness of about 140 MPa $m^{1/2}$ at the yield stress being as high as 1 GPa.

Acknowledgments

The authors acknowledge financial support from the Key Research Program of Frontier Sciences, CAS, National Science Foundation of China (Grant Nos. 51420105001, 51371171, 51471172, 51401211 and U1608257). Z.Y. acknowledges financial support by the Fundamental Research Funds for the Central Universities, China (Grant No. 30915012104) and the Natural Science Foundation of Jiangsu Province, China (Grant No. BK20161498).

References

[1] P. Marshall, Austenitic Stainless Steels: Microstructure and Mechanical Properties, Springer Science & Business Media, 1984.
[2] M.F. Ashby, Materials Selection in Mechanical Design, fourth ed., Butterworth-Heinemann, Burlington, 2010.
[3] X.H. Chen, J. Lu, L. Lu, K. Lu, Tensile properties of a nanocrystalline 316L austenitic stainless steel, Scripta Mater. 52 (2005) 1039–1044.
[4] H. Ueno, K. Kakihata, Y. Kaneko, S. Hashimoto, A. Vinogradov, Nanostructurization assisted by twinning during equal channel angular pressing of metastable 316L stainless steel, J. Mater. Sci. 46 (2011) 4276–4283.
[5] H. Ueno, K. Kakihata, Y. Kaneko, S. Hashimoto, A. Vinogradov, Enhanced fatigue properties of nanostructured austenitic SUS 316L stainless steel, Acta Mater. 59 (2011) 7060–7069.
[6] Olivier Bouaziz, David Barbier, Philippe Cugy, G. Petigand, Effect of process parameters on a metallurgical route providing nano-structured single phase steel with high work-hardening, Adv. Eng. Mater. 14 (2011) 49–51.
[7] G.Z. Liu, N.R. Tao, K. Lu, 316L austenite stainless steels strengthened by means of nano-scale twins, J. Mater. Sci. Technol. 26 (2010) 289–292.
[8] F.K. Yan, G.Z. Liu, N.R. Tao, K. Lu, Strength and ductility of 316L austenitic stainless steel strengthened by nano-scale twin bundles, Acta Mater. 60 (2012) 1059–1071.
[9] S. Scheriau, Z. Zhang, S. Kleber, R. Pippan, Deformation mechanisms of a modified 316L austenitic steel subjected to high pressure torsion, Mater. Sci. Eng., A 528 (2011) 2776–2786.
[10] Q. Xue, E.K. Cerreta, G.T. Gray III, Microstructural characteristics of post-shear localization in cold-rolled 316L stainless steel, Acta Mater. 55 (2007) 691–704.
[11] N.R. Tao, K. Lu, Dynamic plastic deformation (DPD): a novel technique for synthesizing bulk nanostructured metals, J. Mater. Sci. Technol. 23 (2007) 771–774.
[12] Y.S. Li, N.R. Tao, K. Lu, Microstructural evolution and nanostructure formation in copper during dynamic plastic deformation at cryogenic temperatures, Acta Mater. 56 (2008) 230–241.
[13] A. Belyakov, T. Sakai, H. Miura, R. Kaibyshev, K. Tsuzaki, Continuous recrystallization in austenitic stainless steel after large strain deformation, Acta Mater. 50 (2002) 1547–1557.
[14] N. Tsuji, Y. Ito, Y. Saito, Y. Minamino, Strength and ductility of ultrafine grained aluminum and iron produced by ARB and annealing, Scripta Mater. 47 (2002) 893–899.
[15] Y.S. Li, Y. Zhang, N.R. Tao, K. Lu, Effect of thermal annealing on mechanical properties of a nanostructured copper prepared by means of dynamic plastic deformation, Scripta Mater. 59 (2008) 475–478.
[16] X. Zhang, O. Anderoglu, A. Misra, H. Wang, Thermal stability of sputtered Cu films with nanoscale growth twins, J. Appl. Phys. 103 (2008), 094322.
[17] X. Zhang, A. Misra, H. Wang, J.G. Swadener, A.L. Lima, M.F. Hundley, R.G. Hoagland, Thermal stability of sputter-deposited 330 austenitic stainless-steel thin films with nanoscale growth twins, Appl. Phys. Lett. 87 (2005), 233116.
[18] H.T. Wang, N.R. Tao, K. Lu, Strengthening an austenitic Fe–Mn steel using nanotwinned austenitic grains, Acta Mater. 60 (2012) 4027–4040.
[19] K. Lu, F.K. Yan, H.T. Wang, N.R. Tao, Strengthening austenitic steels by using nanotwinned austenitic grains, Scripta Mater. 66 (2012) 878–883.
[20] R. Pippan, A. Hohenwarter, The importance of fracture toughness in ultrafine and nanocrystalline bulk materials, Mater. Res. Lett. 4 (2016) 127–136.
[21] Z. Zeng, X. Li, L. Lu, T. Zhu, Fracture in a thin film of nanotwinned copper, Acta Mater. 98 (2015) 313–317.
[22] Z. You, X. Li, L. Gui, Q. Lu, T. Zhu, H. Gao, L. Lu, Plastic anisotropy and associated deformation mechanisms in nanotwinned metals, Acta Mater. 61 (2013) 217–227.
[23] K. Lu, Stabilizing nanostructures in metals using grain and twin boundary architectures, Nat. Rev. Mater. 1 (2016), 16019.

[24] K. Lu, L. Lu, S. Suresh, Strengthening materials by engineering coherent internal boundaries at the nanoscale, Science 324 (2009) 349–352.
[25] F.K. Yan, N.R. Tao, F. Archie, I. Gutierrez-Urrutia, D. Raabe, K. Lu, Deformation mechanisms in an austenitic single-phase duplex microstructured steel with nanotwinned grains, Acta Mater. 81 (2014) 487–500.
[26] E.W. Qin, L. Lu, N.R. Tao, J. Tan, K. Lu, Enhanced fracture toughness and strength in bulk nanocrystalline Cu with nanoscale twin bundles, Acta Mater. 57 (2009) 6215–6225.
[27] E.W. Qin, L. Lu, N.R. Tao, K. Lu, Enhanced fracture toughness of bulk nanocrystalline Cu with embedded nanoscale twins, Scripta Mater. 60 (2009) 539–542.
[28] S.S. Luo, Z.S. You, L. Lu, Instrinsic fracture toughness of bulk nanostructrued Cu with nanoscale deformation twins, Scripta Mater. 133 (2017) 1–4.
[29] ASTM E1820-11, Standard Test Method for Measurement of Fracture Toughness, American Society for Testing and Materials, Philadelphia (PA), 2011.
[30] L. Xiong, Z.S. You, L. Lu, Fracture behavior of an austenitic stainless steel with nanoscale deformation twins, Scripta Mater. 127 (2017) 173–177.
[31] L. Xiong, Z.S. You, L. Lu, Enhancing fracture toughness of nanotwinned austenitic steel by thermal annealing, Scripta Mater. 119 (2016) 55–59.
[32] ASTM E399-90, Standard Test Method for Plane-strain Fracture Toughness of Metallic Materials, American Society of Testing and Materials, Philadelphia (PA), 1990.
[33] K.S. Kumar, S. Suresh, M.F. Chisholm, J.A. Horton, P. Wang, Deformation of electrodeposited nanocrystalline nickel, Acta Mater. 51 (2003) 387–405.
[34] C. Xiao, R.A. Mirshams, S.H. Whang, W.M. Yin, Tensile behavior and fracture in nickel and carbon doped nanocrystalline nickel, Mater. Sci. Eng., A 301 (2001) 35–43.
[35] G. Lacroix, T. Pardoen, P.J. Jacques, The fracture toughness of TRIP-assisted multiphase steels, Acta Mater. 56 (2008) 3900–3913.
[36] M.F. Ashby, Deformation of plastically non-homogeneous materials, Phil. Mag. 21 (1970) 399–424.
[37] A. Singh, L. Tang, M. Dao, L. Lu, S. Suresh, Fracture toughness and fatigue crack growth characteristics of nanotwinned copper, Acta Mater. 59 (2011) 2437–2446.
[38] M.E. Launey, R.O. Ritchie, On the fracture toughness of advanced materials, Adv. Mater. 21 (2009) 2103–2110.
[39] R.O. Ritchie, The conflicts between strength and toughness, Nat. Mater. 10 (2011) 817–822.
[40] K.S. Kumar, H. Van Swygenhoven, S. Suresh, Mechanical behavior of nanocrystalline metals and alloys, Acta Mater. 51 (2003) 5743–5774.
[41] A. Pineau, A. Amine Benzerga, T. Pardoen, Failure of metals III: fracture and fatigue of nanostructured metallic materials, Acta Mater. 107 (2016) 508–544.
[42] I. Ovid'ko, Review on the fracture processes in nanocrystalline materials, J. Mater. Sci. 42 (2007) 1694–1708.
[43] W.J. Mills, Fracture toughness of type 304 and 316 stainless steels and their welds, Int. Mater. Rev. 42 (1997) 45–82.
[44] J.E. Pawel, D.J. Alexander, M.L. Grossbeck, A.W. Longest, A.F. Rowcliffe, G.E. Lucas, S. Jitsukawa, A. Hishinuma, K. Shiba, Fracture toughness of candidate materials for ITER first wall, blanket, and shield structures, J. Nucl. Mater. 212–215 (Part 1) (1994) 442–447.
[45] R.W. Hertzberg, Deformation and Fracture Mechanics of Engineering Materials, fourth ed., John Wiley & Sons, Inc, 1996.
[46] J.W. Christian, S. Mahajan, Deformation twinning, Prog. Mater. Sci. 39 (1995) 1–157.
[47] Y. Yuan, Y.F. Gu, T. Osada, Z.H. Zhong, T. Yokokawa, H. Harada, A new method to strengthen turbine disc superalloys at service temperatures, Scripta Mater. 66 (2012) 884–889.
[48] Y. Wei, Y. Li, L. Zhu, Y. Liu, X. Lei, G. Wang, Y. Wu, Z. Mi, J. Liu, H. Wang, H. Gao, Evading the strength–ductility trade-off dilemma in steel through gradient hierarchical nanotwins, Nat. Commun. 5 (2014) 3580.